

### Extrinsic toughening in bonded joints with hybrid thermoset-thermoplastic bondline Experimental evidence and modeling strategy

Perdana, Arifian Sandovic; Jusuf, Annisa; Yudhanto, Arief; Lubineau, Gilles; Tao, Ran; Hadi, Bambang Kismono

10.1016/j.compositesa.2024.108686

**Publication date** 

**Document Version** Final published version

Published in

Composites Part A: Applied Science and Manufacturing

Citation (APA)

Perdana, A. S., Jusuf, A., Yudhanto, A., Lubineau, G., Tao, R., & Hadi, B. K. (2025). Extrinsic toughening in bonded joints with hybrid thermoset-thermoplastic bondline: Experimental evidence and modeling strategy. Composites Part A: Applied Science and Manufacturing, 190, Article 108686. https://doi.org/10.1016/j.compositesa.2024.108686

#### Important note

To cite this publication, please use the final published version (if applicable). Please check the document version above.

Copyright

Other than for strictly personal use, it is not permitted to download, forward or distribute the text or part of it, without the consent of the author(s) and/or copyright holder(s), unless the work is under an open content license such as Creative Commons.

Please contact us and provide details if you believe this document breaches copyrights. We will remove access to the work immediately and investigate your claim.

# Green Open Access added to TU Delft Institutional Repository 'You share, we take care!' - Taverne project

https://www.openaccess.nl/en/you-share-we-take-care

Otherwise as indicated in the copyright section: the publisher is the copyright holder of this work and the author uses the Dutch legislation to make this work public.

ELSEVIER

Contents lists available at ScienceDirect

### Composites Part A

journal homepage: www.elsevier.com/locate/compositesa



## Extrinsic toughening in bonded joints with hybrid thermoset—thermoplastic bondline: Experimental evidence and modeling strategy

Arifian Sandovic Perdana <sup>a</sup>, Annisa Jusuf <sup>b,o</sup>, Arief Yudhanto <sup>c,d,o</sup>, Gilles Lubineau <sup>d,o</sup>, Ran Tao <sup>e,o</sup>, Bambang Kismono Hadi <sup>b,o</sup>

- <sup>a</sup> Aerospace Engineering Study Program, Faculty of Mechanical and Aerospace Engineering, Institut Teknologi Bandung (ITB), Bandung, Indonesia
- b Mechanics of Solids and Lightweight Structures Research Group, Faculty of Mechanical and Aerospace Engineering, Institut Teknologi Bandung (ITB), Bandung, Indonesia
- <sup>c</sup> Department of Mechanical Engineering, School of Engineering and Computer Science, Baylor University, Waco, Texas, USA
- <sup>d</sup> Mechanics of Composites for Energy and Mobility Laboratory, Mechanical Engineering Program, Physical Sciences and Engineering Division, King Abdullah University of Science and Technology (KAUST), Thuwal, Saudi Arabia
- e Faculty of Aerospace Engineering, Structural Integrity & Composites, Delft University of Technology, Delft, The Netherlands

#### ARTICLE INFO

# Keywords: Composite bonded joints Finite element Mode-I fracture Energy release rate

#### ABSTRACT

Adhesive bonded composite joints with an embedded insert consisting of an interfacial hybrid thermoset-thermoplastic bondline could activate an extrinsic toughening mechanism that quadruples the mode I fracture toughness. However, the mechanisms of extrinsic toughening (anchoring, debonding, stretching, detachment), their associated energy dissipation, and the role of bondline parameters (wavelength, porosity, ductility) have not been detailed thus far. Here, we developed double cantilever beam (DCB) finite element models consisting of two rigid composite adherends and an elastoplastic bondline. We prescribed a spatially arranged interfacial/cohesive pattern to simulate the extrinsic toughening and evaluate the increase in fracture toughness. DCB tests were performed to validate the load–displacement curves, fracture toughness, and extrinsic toughening mechanisms obtained from the finite element models. The elastic–plastic energy dissipation during the crackbridging process was also evaluated using the models. Despite the two-dimensional nature, the modeling results are in reasonable agreement with the experiments, providing an option for further developing a new heterogeneous bondline concept.

#### 1. Introduction

Composite materials are used to manufacture aerospace and automotive parts due to their weight-saving capability and strength- or stiffness-to-weight ratio. Bonding between composite parts becomes an inevitable way to reduce the structural weight further [1–5]. Unlike mechanically bolted or riveted joints, adhesive bonded joints can alleviate a premature failure generally caused by the stress concentration around the hole in bolted/riveted joints [6,7]. However, using adhesive bonded joints poses the risks of adhesive degradation, voided bondline, weak adherend-adhesive interfaces, and poor surface treatment [8,9]. Therefore, methods to improve the strength and toughness of bonded joints have been sought by relying on different engineering concepts.

The methods developed to improve the mechanical performance of adhesively bonded joints include adherend treatment by surface patterning, bondline modification via additive concept (hybrid bonding [10–12], soft interlayer, interleave, heterogeneous [13]), and subtraction concept (adhesive voiding [14]). The methods generally aim

to inhibit delamination growth by activating an additional energy dissipation due to the crack-bridging feature on the wake of a crack, i.e., extrinsic toughening [15–17]. Here, in a system experiencing extrinsic toughening, the crack-bridging features (ligaments, strands) reduce the local stresses or strains at the crack tip as the features bear some of the applied load [18]. Some examples of crack-bridging features/mechanisms include crack-path deviation [19], crack bridging by substrate ligament [20–22], adhesive ligament [23], metallic mesh [11,24], and thermoplastic carrier [10,12,25–27]. In the case of a thermoplastic carrier, a more ductile ligament was postulated to improve further the plastic energy dissipation during the ligament stretching [12]. However, detailed crack-bridging mechanisms and energy dissipation in bonded joints with hybrid adhesives that can improve fracture toughness are still unknown.

This study aims to develop a simple finite element model incorporating a hybrid thermoset–thermoplastic bondline that simulates the

E-mail address: annisa.jusuf@itb.ac.id (A. Jusuf).

<sup>\*</sup> Corresponding author.

Table 1

Type of samples used in the experiments. Note: P stands for plain (sample without inserts); L stands for the wavelength of wavy spacing; W stands for the adhesive weight used to bond the sample.

Sample code	Bondline configuration	Wavelength (mm)	Adhesive feature
P	Without insert	-	Saturated (30 g)
L20-W14	With insert	20	Non-saturated (14 g)
L20-W30	With insert	20	Saturated (30 g)
L40-W14	Without insert	40	Non-saturated (14 g)
L40-W30	Without insert	40	Saturated (30 g)

mode I fracture behavior of DCB test specimens reported in Ref. [12]. The two-dimensional models were developed in commercial software. ABAOUS/CAE, to understand the mechanisms behind the extrinsic toughening. To date, modeling efforts in this direction have been rarely found in the literature, especially when considering the effect of wavelength, porosity, and thermoplastic properties. The absence of models, albeit the simplified one, to simulate the global response, energy release rate, energy dissipation, and crack-bridging mechanism of DCB with a hybrid bondline has not been proposed thus far. To this end, instead of explicitly building a wavy bondline, we resorted to prescribing the spatially arranged interface segments that could trigger ligaments, inspired by the methods developed in Refs. [23,28]. By alternating the interface segments on two opposite sides of the bondline using two configurations, i.e., strong-weak interfaces and strong-moderate interfaces (interfacial patterning), the formation of bridging strands as the basis of bridging mechanisms was simulated.

The remainder of this paper is organized as follows. Section 2 describes the experimental methods, including the materials, processing techniques, mode I fracture test method (double cantilever beam), and material and adhesion properties identification. Section 3 describes the modeling strategy, which consists of an overview of the model, cohesive element zone modeling, and models developed for a bonded joint with thermoset and hybrid thermoset–thermoplastic bondlines. Section 4 presents the results obtained from modeling and simulation, validated by the experimental results, and discusses the role of thermoplastic properties in activating extrinsic toughening. Conclusions are given in Section 5, providing the main scientific findings of the model.

#### 2. Experimental methods

#### 2.1. Materials and manufacturing

The specimen used in the experiments consists of three main parts: adherend, insert, and adhesive. We used carbon/epoxy (CFRP) pre-preg (T700/M21 Hexply from Hexcel) with 0.125 mm thickness to manufacture the adherend with a stacking sequence of [0]8. The stacked CFRP prepregs were consolidated in a vacuum bag with 1-bar pressure that was compressed using a static press (Pinette Emidecau Industries 15T) at 7 bar and 180 °C for 2 h [12]. Once cured, the carbon/epoxy panel was cut into smaller-sized specimens using a waterjet cutter. The dimension of each sample was 250 mm × 20 mm. The insert was made of thermoplastic (polyamide-6) with a wavy microstructure 0.8 mm thick using an additive manufacturing (AM) technique, i.e., 3D printer (BCN3D Sigma). AM technique has been increasingly used to fabricate a complex part [29] for enhancing joint strength [30,31], toughness [32], and fatigue response [33]. We additive manufactured the insert and weft separately and manually weaved them to provide a 'wavy' microstructure; see the details in Ref. [12]. The wavy microstructure was designed to break the symmetry, providing spatially varying connections between CFRP adherends. The adhesive used to bond CFRP adherends and polyamide-6 insert was epoxy (Araldite 420 A/B, Huntsman) with a weight mixing ratio of 10:4.

Each sample was prepared by, first, treating the surface of carbon/epoxy using CO $_2$  laser (wavelength =  $10.6\,\mu m$ , fluence =  $3.2\,J/cm^2$ , speed =  $500\,mm/s$ , pulse frequency =  $20\,kHz$ , power =  $22.5\,J$ ; PLS6.75 Laser Platform, Universal Laser Systems). These settings have been optimized to effectively remove the contaminants and selectively remove

the matrix layer from the composite surface, producing multiple bare fibers ready to be bonded with adhesive. The laser-treated surface was then cleaned with acetone in an ultrasonic cleaner (Branson 8510) and dried at 60 °C for 30 min. An epoxy adhesive (Araldite 420 A/B, Huntsman) was then spread on the surface of one carbon/epoxy sample. The amount of adhesive was determined based on the qualitative observation of pores on the bondline of bonded specimens using Xray micro-computed tomography. Note that the size and distribution of pores (i.e., porosity) in the bondline could not be strictly controlled quantitatively. The parameters in the process that can help define the porosity qualitatively are the adhesive amount, vacuum condition, and mesh size of the insert. Therefore, porosity variation among samples was expected. The amount of adhesive was varied according to the weight, i.e., 30 g (a saturated amount of adhesive) and 14 g (a nonsaturated amount of adhesive). We also varied the wavelength of the insert, i.e., 20 mm (short wavelength) and 40 mm (long wavelength). The wavy insert was manually laid on the top surface of a CFRP adherend already coated with a thin epoxy layer. The PA-6 insert and epoxy adhesive were then sandwiched between two CFRP adherends. The sample types used in the experiments are summarized in Table 1.

#### 2.2. Identification of material properties

We performed an extensive experimental campaign to identify carbon/epoxy adherend material properties, bondline (epoxy adhesive, polyamide-6 insert), and interfaces. The experimental protocols used to identify these properties can be reviewed in Refs. [12]. All these properties were employed in the models described in Section 3.

Tensile and shear tests were performed to obtain tensile moduli, Poisson's ratio, and shear moduli on carbon/epoxy adherend as follows:  $E_{xx}$  of 125 GPa,  $E_{yy}$  (=  $E_{zz}$ ) of 7.8 GPa,  $v_{xy}$  (=  $v_{xz}$ ) of 0.33,  $v_{yz}$  of 0.4,  $G_{xy}$  (=  $G_{xz}$ ) of 5.1 GPa,  $G_{yz}$  of 2.8 GPa. The mechanical properties of the epoxy adhesive used in the simulation are given as follows: E of 1.5 GPa, yield stress  $G_y$  of 26 MPa, ultimate stress  $G_y$  of 35 MPa, yield strain of  $E_y$  of 1.8%, failure strain of  $E_y$  of 5.2%. The 3D-printed PA-6 insert have the following properties: E of 0.3 GPa, yield stress  $G_y$  of 20 MPa, ultimate stress  $G_y$  of 44 MPa, yield strain of  $E_y$  of 22%, failure strain of  $E_y$  of 140%.

Interface properties were obtained by performing floating roller tests on composite-epoxy-composite and epoxy-polyamide-6 (PA-6) interfaces, i.e., energy release rate  $G_c$ . In addition, single-lap joint and three-point bending tests were also performed on the composite-epoxy-composite interface. We categorized the cohesive element properties as follows: 'weak' ( $G_c = 0.15 \text{ N/mm}$ ,  $\tau^0 = 15 \text{ MPa}$ ), 'moderate' ( $G_c = 0.51 \text{ N/mm}$ ,  $\tau^0 = 19 \text{ MPa}$ ), and 'strong' ( $G_c = 2.46 \text{ N/mm}$ ,  $\tau^0 = 37 \text{ MPa}$ ). The description of 'weak' cohesive was based on the poor interfacial strength and toughness from the adhesion properties between two composite surfaces after peel-ply treatment [23]. The description of 'strong' and 'moderate' cohesive was obtained floating roller test experiments [12]. Note that the typical values of  $G_c$  and  $\tau^0$  employed for DCB models are 0.969 N/mm and 5–40 MPa, respectively [34].

#### 2.3. Mode I fracture test for validation

Mode I fracture test was measured using a double cantilever beam (DCB) specimen shown in Fig. 1a, where the thermoplastic insert and

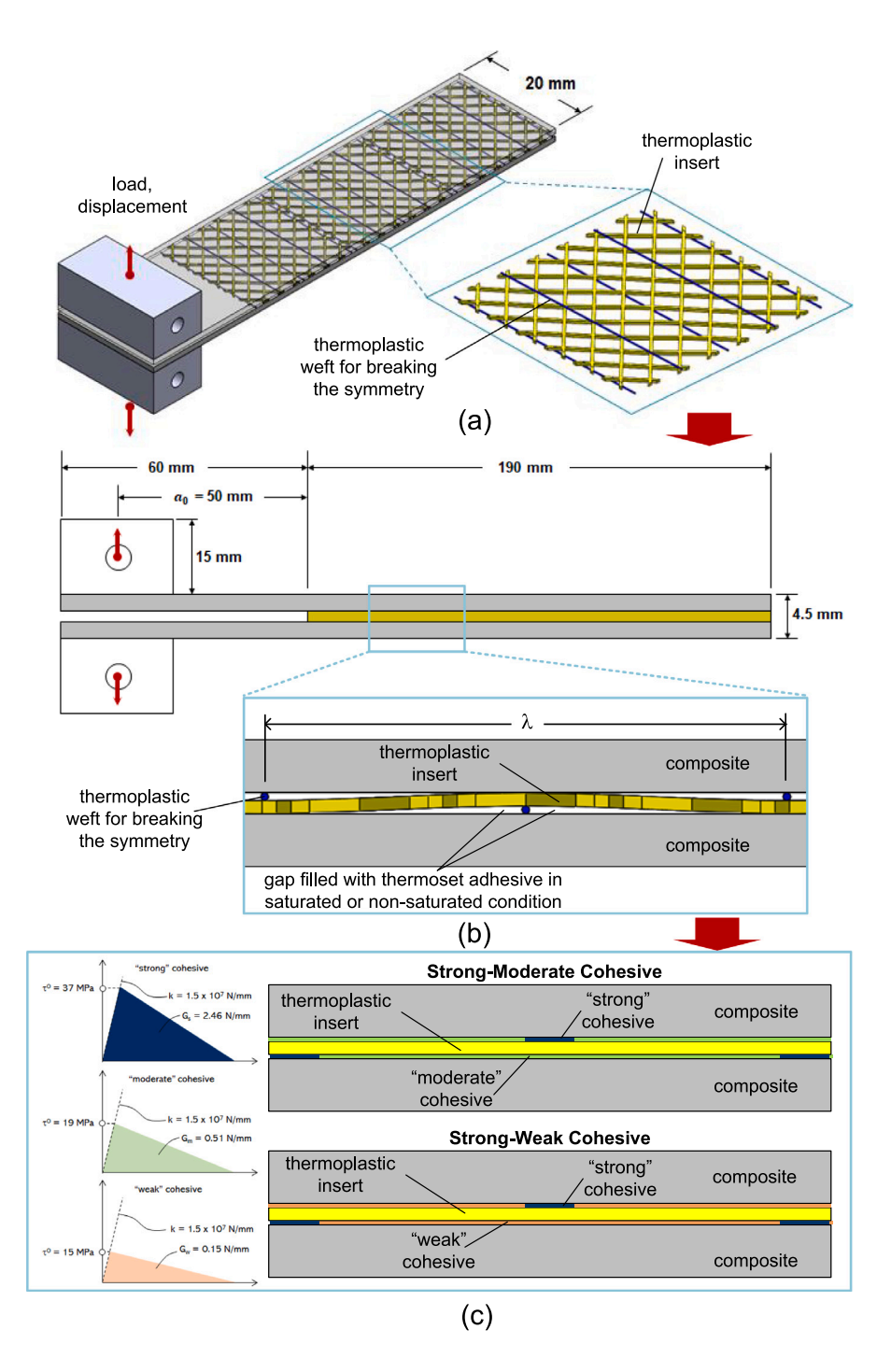


Fig. 1. (a) Schematics of double cantilever beam (DCB) specimen with thermoplastic insert and thermoplastic weft intended for breaking the symmetry and creating 'wavy' bondline, (b) 2D model of DCB specimen with wavy bondline, (c) conversion of wavy bondline into a flat bondline with the spatial combination of either strong-moderate or strong-weak cohesive elements.

wefts are depicted here. The DCB specimen has a length of 250 mm and a width of 20 mm. Fig. 1b shows the side view of the DCB specimen. The distance between two upper weft lines prescribed the wavelength of the waviness  $\lambda$ , which was either 20 or 40 mm. The DCB tests were performed on two main configurations, namely specimens without insert (composites were purely bonded using epoxy with a thickness of 0.8 mm) and specimens with insert (saturated adhesive,  $\lambda = 20$  mm; saturated adhesive,  $\lambda = 40$  mm; non-saturated adhesive,  $\lambda = 20$  mm;

non-saturated adhesive,  $\lambda=40$  mm). We adopted protocols given in the ASTM D5528 for measuring the energy release rate  $G_{Ic}$  using compliance calibration [35,36] as follows:

$$G_{IC} = \frac{nP\delta}{2Ba} \cdot \frac{F}{N} \tag{1}$$

where P is the force,  $\delta$  is the displacement, B is the specimen width, a is the crack length, n is the exponential value of the slope between  $\log(a)$  in the y-axis and  $\log(\delta/P)$  in the x-axis, F and N are the correction

factors for large displacement and loading blocks, respectively, when  $\delta/a > 0.4$ .

#### 3. Modeling strategy

#### 3.1. General description of FE models

A two-dimensional double cantilever beam finite element (FE) model consisting of the adherend, bondline, and cohesive elements was built in ABAQUS/CAE. The beam dimension was 250 mm long and 20 mm wide, while the pre-crack length  $a_0$  was 50 mm. Two main models were developed: bonded joint model with thermoset bondline (bondline thickness of 0.5 and 0.8 mm) and bonded joint model with thermoset-thermoplastic bondline (bondline thickness of 0.5 mm). Two aluminum blocks (length of 20 mm, height of 15 mm) were also built on the upper and lower end-points of the model. The blocks were made of rigid body elements, facilitating displacementcontrolled loading increments in the upper block and pinned boundary conditions in the lower block. The reduced integration and enhanced hourglass control were activated to ensure efficient computational time and numerical convergence. Geometrical non-linearity (NLGEOM) was also activated to accommodate the non-linear phenomena during the simulation. Cohesive elements were prescribed between the bondline and adherends to model the adhesive response [37], which is discussed in Section 3.2. To obtain the R-curve from the simulation, we employed the compliance calibration technique as described in Eq. (1) to obtain the  $G_{Ic}$  value. The force P was the reaction force at the loading point in the model, while the displacement  $\delta$  was the corresponding displacement at the loading pin. The crack length a was calculated as the distance between the loading point and the crack front (location of the 'damaged' cohesive element, i.e., when d is lower than 1) [23]. Note that the FE models were all developed in commercial software, i.e., ABAQUS/CAE, to enable the quick analysis of results, streamlining the optimization of materials and geometrical information of the bondline features.

#### 3.2. Cohesive zone modeling for the interface

The cohesive zone model (CZM) represented the adherend and bondline interface. The physical connection representing the adherend-bondline interface was the cohesive element with 0.1-µm thickness that obeyed a bi-linear traction–separation law. The relationship between traction  $\tau$  and separation  $\delta$  is expressed as follows

$$\begin{cases} \tau_n \\ \tau_s \\ \tau_t \end{cases} = \begin{bmatrix} K_{nn} & 0 & 0 \\ 0 & K_{ss} & 0 \\ 0 & 0 & K_{tt} \end{bmatrix} \begin{cases} \delta_n \\ \delta_s \\ \delta_t \end{cases}$$
 (2)

where  $\tau_n$ ,  $\tau_s$ , and  $\tau_t$  represent normal (mode I fracture), shear (mode II fracture), and tear (mode III fracture) tractions, respectively; [K] represent the stiffness of the cohesive element with the value of  $1.5 \times 10^7$  N/mm<sup>3</sup>, which was already calibrated in Ref. [23]. The damage initiation was triggered by the maximum stress criteria, i.e., if one of the normalized stresses is exceeded, then the damage starts [38]:

$$\max \left\{ \frac{\langle \tau_n \rangle}{\tau_n^0}, \frac{\tau_s}{\tau_s^0}, \frac{\tau_t}{\tau_t^0} \right\} = 1 \tag{3}$$

 $\tau_n^0$ ,  $\tau_s^0$ , and  $\tau_t^0$  represent the critical stresses for each fracture mode. This criterion was selected based on the conservative assumption that a specific mode controls the fracture/delamination process zone, and the role of mode mixity is not considered. This simplified approach was sufficiently effective for our DCB case because the mode-I component was expected to dominate the damage process. Other damage initiation criteria, such as quadratic nominal stress [39], can certainly be employed for representing brittle adhesive. Once the critical stress is

exceeded, the degradation of the cohesive element is represented by a linear degradation of damage [38,40] as follows

$$d = \frac{\delta^f(\delta^c - \delta^0)}{\delta^c(\delta^f - \delta^0)} \tag{4}$$

where d is the damage variable (ranging from 0 to 1);  $\delta^0$ ,  $\delta^c$ , and  $\delta^f$  represent the initial, current, and maximum separation, respectively, of the cohesive elements upon loading. The area under the bi-linear curve represents the fracture toughness, namely  $G_n^c$ ,  $G_n^c$ , and  $G_n^c$ , which are the critical energy release rates in normal, shear, and tear, respectively.

#### 3.3. Models with thermoset and hybrid thermoset-thermoplastic bondlines

Two models representing DCB specimens with thermoset and hybrid thermoset-thermoplastic bondlines were developed in this study. The first model (model with thermoset bondline) was used to study the effect of bondline thicknesses (0.5 and 0.8 mm) and cohesive toughness (low and moderate toughness so-called 'weak' and 'moderate' interfaces, respectively). The  $G_c$  values prescribed for weak and moderate interfaces were 0.15 and 0.51 N/mm, respectively. The modeling outcome from the model with 0.8-mm bondline thickness was compared with the experiments. The second model (model with hybrid bondline) was used to reveal the effect of wavelength and cohesive toughness and the crack-bridging mechanisms. Note that the bondline thickness for a model with a hybrid bondline was 0.5 mm, which is the thickness of the flat insert (eliminating the thermoplastic weft). This simplification was described by the transformation from a naturally wavy insert (Fig. 1b) into a flat bondline with spatially correlated cohesive segments (Fig. 1c). Here, two combinations for the spatially correlated cohesive segments were proposed: (i) strong-moderate (combination of 2.46 N/mm and 0.51 N/mm; ratio of 4.8), and (ii) strong-weak (combination of 2.46 N/mm and 0.15 N/mm; ratio of 16.4). The segment length of the strong cohesive was 0.3 mm, adopting the diameter of the thermoplastic weft. The distance between two strong, cohesive segments represented the distance between two 'anchor' points and was determined based on the insert's nominal wavelength  $\lambda$  (20 or 40 mm). The finite element model configurations are summarized in Table 2. The bi-linear traction-separation laws describing 'strong', 'moderate', and 'weak' cohesive/interface are given in Fig. 1c.

#### 4. Results and discussion

#### 4.1. Bonded joints with thermoset bondline

#### 4.1.1. Load-displacement curves

The comparison of force-displacement  $(P-\delta)$  between experiments and finite element models (with 'moderate' and 'weak' cohesive, and with 0.5-mm and 0.8-mm thick epoxy bondline) is shown in Fig. 2a. The DCB experiments produced a slight variation of load-displacement slope and the peak force (55-73 N) due to geometrical differences among samples (initial crack length) as commonly observed in similar settings [41]. Nonetheless, FE models could emulate the global response of the DCB experiments, starting from the linear load-displacement slope, peak force, and the ensuing decay of load. FE models with moderate cohesive ( $G_c = 1.51 \text{ N/mm}$ ) produced a linear force-displacement, reaching 75-80 N force, followed by the gradual decay of force. On the other hand, FE models with weak cohesive ( $G_c$ = 0.51 N/mm) produced a peak load that is 30%-35% lower than moderate cohesive. FE simulation also shows that with the same value of Gc of either 0.51 N/mm or 1.51 N/mm, DCB models with 0.8 mm and 0.5 mm thick bondlines exhibited identical force-displacement responses.

#### 4.1.2. Energy release rate

The effect of cohesive toughness and bondline thickness on the energy release rate  $G_{Ic}$  is shown in Fig. 2b. The DCB experiments (with

**Table 2**Type of finite element models used in the simulation. Note: P stands for plain (sample without inserts); L stands for the wavelength of wavy spacing (note that L is interchangebly with  $\lambda$ ); SW stands for strong-weak cohesive element combination; SM stands for strong-moderate cohesive element combination.

Model code	Bondline properties	Bondline thickness (mm)	Wavelength (mm)	Cohesive feature
P0.8-W	Adhesive	0.8	_	Weak
P0.8-M	Adhesive	0.8	_	Moderate
P0.5-W	Adhesive	0.5	_	Weak
P0.5-M	Adhesive	0.5	_	Moderate
L20-SW	Polyamide-6	0.5	20	Strong-Weak
L20-SM	Polyamide-6	0.5	20	Strong-Moderate
L40-SW	Polyamide-6	0.5	40	Strong-Weak
L40-SM	Polyamide-6	0.5	40	Strong-Moderate

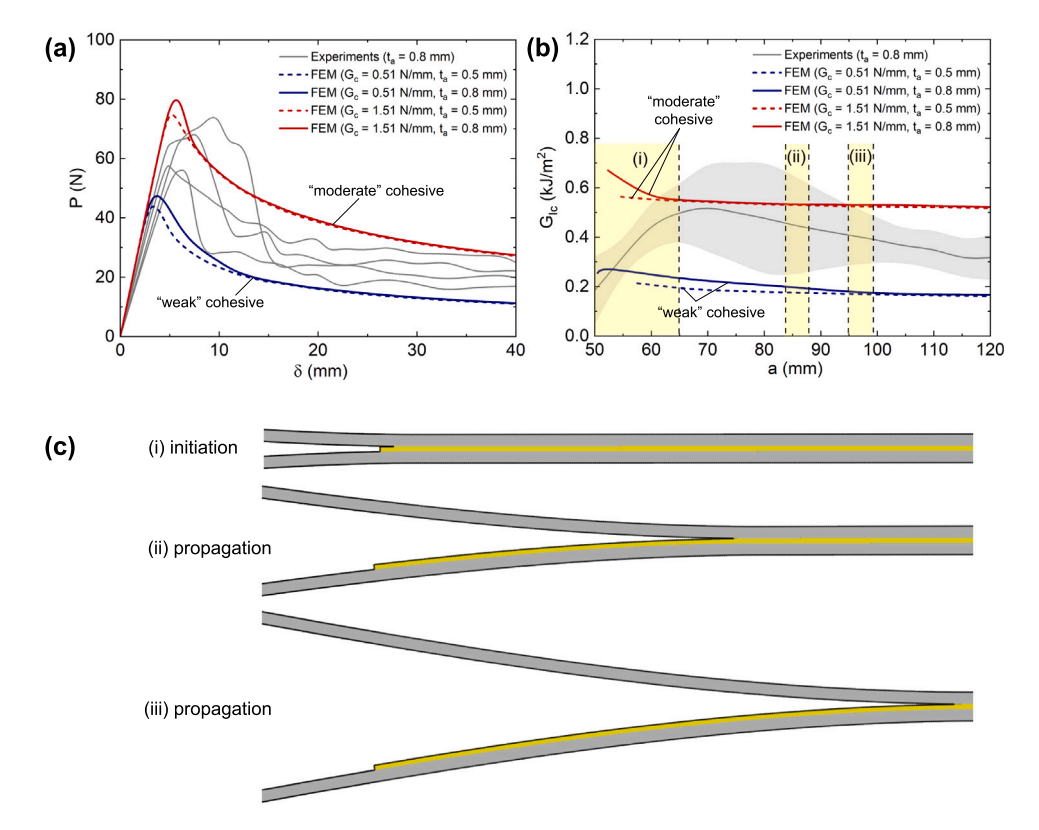


Fig. 2. Bonded joints with thermoset bondline: (a) force-displacement curves, (b) mode I energy release rate  $G_{Ic}$ , (c) simulated delamination growth.

bondline thickness of 0.5 mm) exhibit  $G_{Ic}$  of approximately 0.40 kJ/m² during propagation, spanning from 70 to 120 mm. A slight increase of  $G_{Ic}$  between 60 and 70 mm was due to the variation of peak load, crack length measurement at the initiation stage, and the adhesive spill at the crack initiation point. Here, the FE models with moderate and weak cohesive elements could reproduce the energy release rate obtained from the DCB experiments, providing so-called 'upper and lower bounds' of fracture toughness for the experimental ones. The upper bound (moderate cohesive) and lower bound (weak cohesive) models produced  $G_{Ic}$  of 0.55 and 0.22 kJ/m², respectively, showing that  $G_{Ic}$  of moderate cohesive is almost triple as compared to that of the weak cohesive.

#### 4.1.3. Delamination mechanism

Fig. 2c shows the initiation stage (i) and propagation stages (ii, iii) obtained from the models. As both moderate and weak cohesive models exhibited similar failure modes, we only show one example here, i.e., the moderate one. The failure mode is essentially a delamination at the interface between adhesive bondline and composite adherends (adherend-adhesive failure). This delamination is controlled by the pre-defined cohesive properties (fracture toughness, fracture strength) rather than geometry (adhesive thickness), which is consistent with the

finding reported by Fernandes et al. [42]. Thus, for the models with thermoset–thermoplastic bondline, we used a 0.5-mm thick bondline.

#### 4.2. Bonded joints with hybrid thermoset-thermoplastic bondline

#### 4.2.1. Load-displacement curves

Fig. 3a-d shows the comparison of force-displacement curves between experiments and FEM. The experiments show that embedding a hybrid bondline into bonded joints improved the initial peak force (the onset of crack initiation), reaching the 100-135 N range. The force abruptly decreased once the crack was initiated due to the crack extension. When the ligaments of the PA-6 insert are stretched, the force gradually increases. The stretching and breaking of the ligaments introduce a saw-toothed profile in the force-displacement curve. This force oscillation is associated with a stick-slip phenomenon (i.e., load fluctuation during the crack or delamination propagation at the interface characterized by the crack bridging and trapping [41]). As shown in 3a-d, our FE models could emulate the global mechanical response of the DCB specimens obtained from experiments. When  $\lambda$  was increased from 20 mm to 40 mm (see comparison between Fig. 3a-b and Fig. 3cd), FE models were able to simulate a lower oscillation frequency in the models with  $\lambda = 40$  mm, suggesting that less bridging actions have

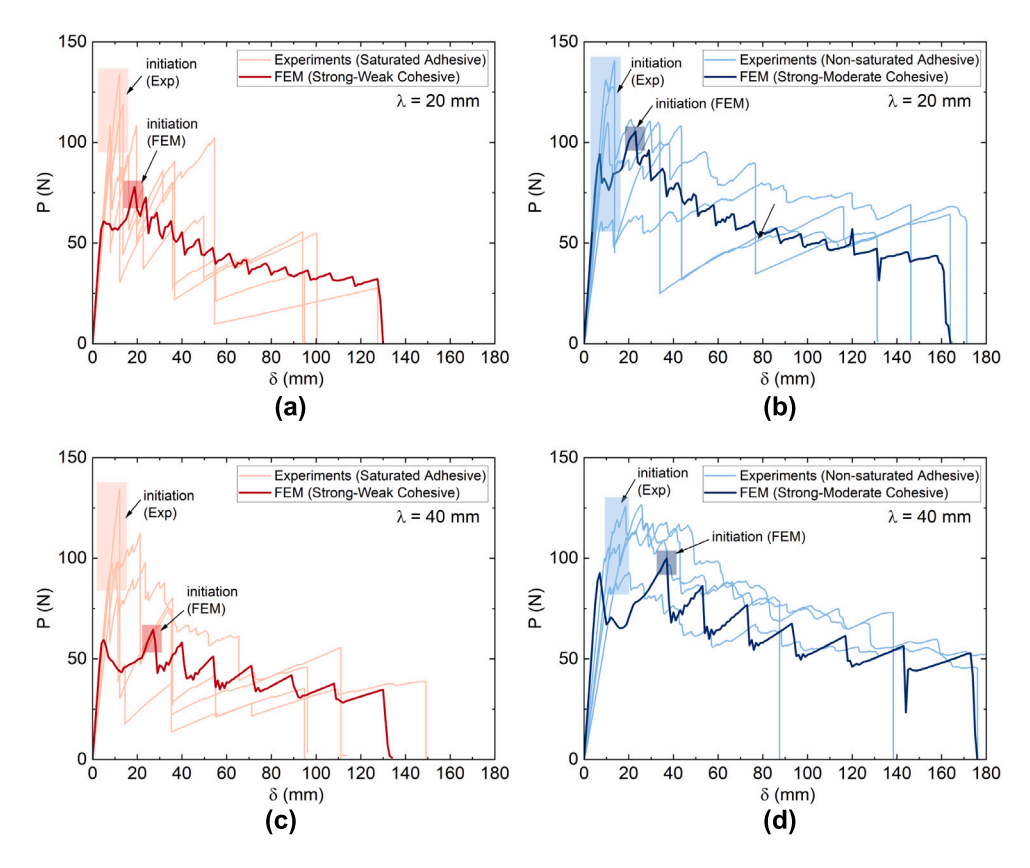


**Fig. 3.** Bonded joints with hybrid thermoset–thermoplastic bondline, comparison of force–displacement curves between experiments and FEM: (a)  $\lambda = 20$  mm (weak cohesive, saturated adhesive), (b)  $\lambda = 20$  mm (moderate cohesive, non-saturated adhesive), (c)  $\lambda = 40$  mm (weak cohesive, saturated adhesive), (d)  $\lambda = 40$  mm (moderate cohesive, non-saturated adhesive).

taken place in these models, which is consistent with the finding in Ref. [43]. In addition, FE models were also able to reasonably simulate the experimentally observed stick–slip phenomenon. However, the crack propagation onset of the FE models starts in the displacement range of 20–40 mm, while that in experiments occurs between 5 and 20 mm (see shaded regions in 3a-d). Our finite element approach developed here is a two-dimensional approximation of the originally three-dimensional nature of the hybrid thermoset–thermoplastic bond-line. The actual experimental event during the crack propagation onset could not be entirely simulated using 2D FE models, e.g., the crack initiation, propagation onset, and breakage of multiple ligaments.

#### 4.2.2. Energy release rate

Fig. 4a-d shows the comparison of Mode I energy release rate  $G_{Ic}$  between experiments and FEM for  $\lambda=20$  mm and  $\lambda=40$  mm. Note that four DCB samples were tested during the experiment, and the R-curve for each sample is shown in Fig. 4a-d along with the average value (dashed line) and standard deviation (shaded area). The experiments showed that the hybrid thermoset–thermoplastic bondline could enhance the mode I fracture toughness of up to  $2.6 \text{ kJ/m}^2$  using  $\lambda=40$  and non-saturated adhesive, culminating in the increase of 400% as compared to the baseline configuration. The attainable  $G_{Ic}$  is also higher than that in composite joints using aerospace-grade epoxy (FM300-2M), which ranges from  $1.0 \text{ to } 1.3 \text{ kJ/m}^2$  [44]. However, the R-curve during experiments typically oscillates, mainly controlled by the random formation of strands during the crack-bridging process.

FEM models, in general, were able to emulate the R-curves of all configurations, simulating the stages of initiation, a gradual increase of fracture toughness, and toughness oscillation during the propagation stage. At the initiation stage, Fig. 4a-b shows that the initial  $G_{Ic}$  of bonded joints with  $\lambda=20$  mm in the experiments is 0.75 kJ/m² (saturated adhesive) and 0.90 kJ/m² (non-saturated adhesive), respectively. In Fig. 4a-b, FE simulation produced initial  $G_{Ic}$  of 0.25 kJ/m²

(strong-weak cohesive) and 0.85 kJ/m<sup>2</sup> (strong-moderate cohesive) to represent saturated and non-saturated adhesive, respectively. After that,  $G_{Ic}$  oscillates due to the activation of crack-bridging strands, which is the primary source of extrinsic toughening and associated with the stick-slip phenomenon [41]. During the propagation stage, as shown in Fig. 4a-b, experimental  $G_{Ic}$  of bonded joints with  $\lambda$  = 20 mm is  $0.9 \text{ kJ/m}^2$  (saturated adhesive) and  $2.4 \text{ kJ/m}^2$  (non-saturated adhesive). FEM shows that the simulated  $G_{Ic}$  for models with  $\lambda$  = 20 mm is 1.1 kJ/m<sup>2</sup> (strong-weak cohesive) and 1.9 kJ/m<sup>2</sup> (strongmoderate cohesive). The R-curve of DCB experiments with  $\lambda = 40$  mm is shown in Fig. 4c-d, depicting initial  $G_{Ic}$  of 0.75 kJ/m<sup>2</sup> (saturated adhesive) and 1.4 kJ/m<sup>2</sup> (non-saturated adhesive). Models with  $\lambda$  = 40 mm show 0.30 kJ/m<sup>2</sup> and 0.80 kJ/m<sup>2</sup> for strong-weak cohesive and strong-moderate cohesive, respectively. Fig. 4c shows that  $G_{Ic}$  in bonded joints with  $\lambda = 40$  mm (saturated adhesive) is 1.0 kJ/m<sup>2</sup>, while the FEM produced  $G_{Ic}$  of 1.1 kJ/m<sup>2</sup> (strong-weak cohesive). As shown in Fig. 4d,  $G_{Ic}$  propagation obtained from experiments with  $\lambda = 40$  mm non-saturated adhesive were 2.6 kJ/m<sup>2</sup>, while that of FEM was 2.1 kJ/m<sup>2</sup>. Our modeling shows that the variation of adhesive content in a hybrid thermoset–thermoplastic bondline can be simulated using the combination of strong-weak or strong-moderate cohesive pattern.

#### 4.2.3. Crack-bridging mechanism during delamination

Our observation on the experimental findings in the composite bonded joints with hybrid thermoset–thermoplastic bondline concluded that the improved  $G_{Ic}$  is associated with the bridging traction provided by the thermoplastic strands. The crack-bridging mechanisms are exemplified using the DCB specimen with  $\lambda=40$  mm (saturated adhesive) and FE model with  $\lambda=40$  mm (strong-weak cohesive) shown in Fig. 5a and b, respectively.  $G_{Ic}$  of model with  $\lambda=40$  mm and saturated adhesive has an average value of 0.75 kJ/m² (initiation) and 1.0 kJ/m² (propagation). However, a significant deviation of  $G_{Ic}$  exists in the experiments. As shown in Fig. 5a, one specimen shows an

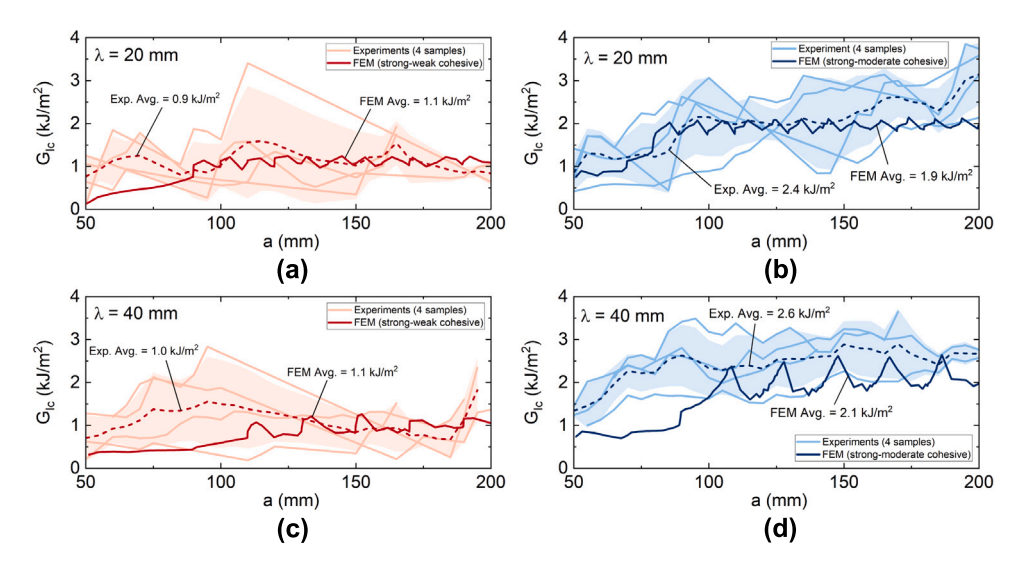


Fig. 4. Bonded joints with hybrid thermoset-thermoplastic bondline, comparison of Mode I energy release rate  $G_{Ic}$  between experiments and FEM: (a)  $\lambda=20$  mm (weak cohesive, saturated adhesive), (b)  $\lambda=20$  mm (moderate cohesive, non-saturated adhesive), (c)  $\lambda=40$  mm (weak cohesive, saturated adhesive), (d)  $\lambda=40$  mm (moderate cohesive, non-saturated adhesive). Note: The shaded area indicates the standard deviation of the data.

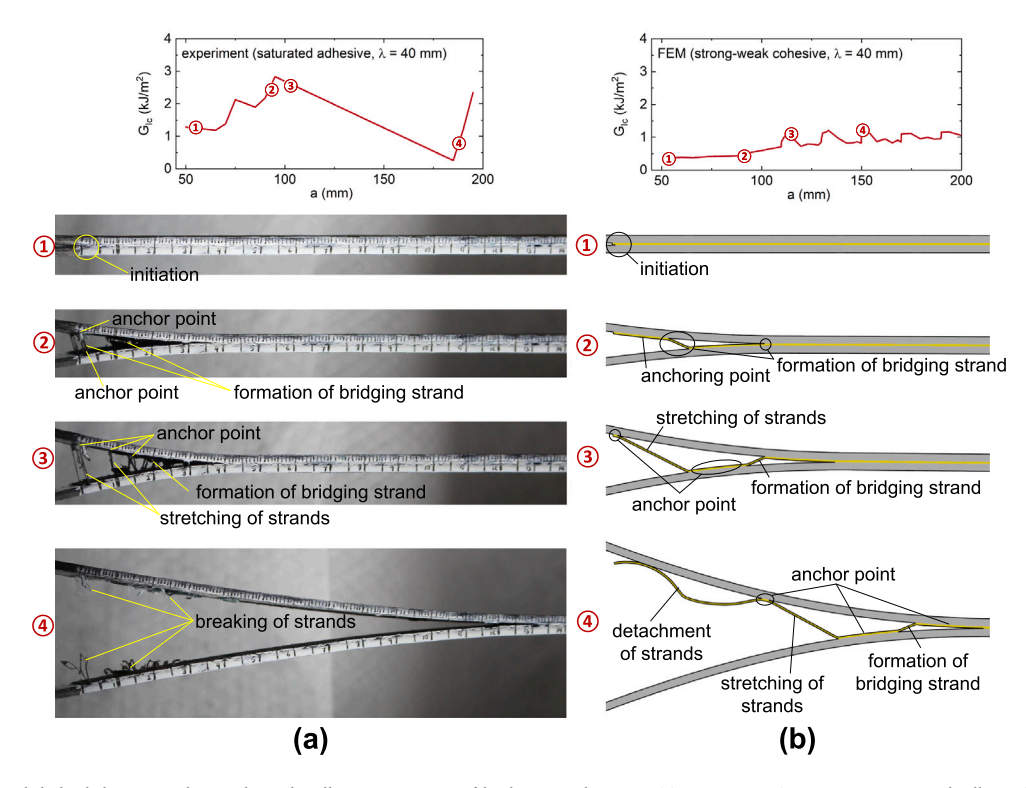


Fig. 5. Bonded joints with hybrid thermoset–thermoplastic bondline, comparison of bridging mechanisms: (a) experiment ( $\lambda = 40$  mm, saturated adhesive), (b) FEM ( $\lambda = 40$  mm, strong-weak cohesive).

initial  $G_{Ic}$  of 1.2 kJ/m² that is increasing to 2.5 kJ/m², and suddenly decreasing to 0.2 kJ/m² due to crack-bridging by the strands and their detachment from substrates. Fig. 5a also shows the relationship between  $G_{Ic}$  modification and associated mechanisms, including crack initiation, formation of bridging strands anchored on the substrates (anchor point), stretching, and breaking or detachment of bridging strands.  $G_{Ic}$  at the initiation stage is associated with the modified bondline properties due to thermoset insert (stage ①). After that, the gradual increase of  $G_{Ic}$  from stage ① to stage ② is characterized by the formation of bridging strands of thermoplastic inserts. Bridging strands were typically pivoted to the 'anchor points' that stem from the strong bonding in the composite|epoxy|nylon connection. A rather stable

condition between stage ② and stage ③ corresponds to the stretching of bridging strands. A gradual decrease of  $G_{Ic}$  is associated with breaking strands from a minimal number of anchor points (stage ③ to stage ④). Here, the thermoset adhesive confined the thermoplastic insert, causing a relatively short bridging strand that broke early. Fig. 5b shows  $G_{Ic}$  of DCB models with  $\lambda=40$  mm for strong-weak cohesive, which is averaging at 0.4 kJ/m² (initiation, ①), increasing stage ②, and stable stage at 1.1 kJ/m² (propagation, ③-④). The model could also simulate the oscillation of fracture toughness with a relatively constant amplitude.

The comparison of the crack bridging mechanism in the DCB specimen with non-saturated adhesive and FE model with strong-moderate

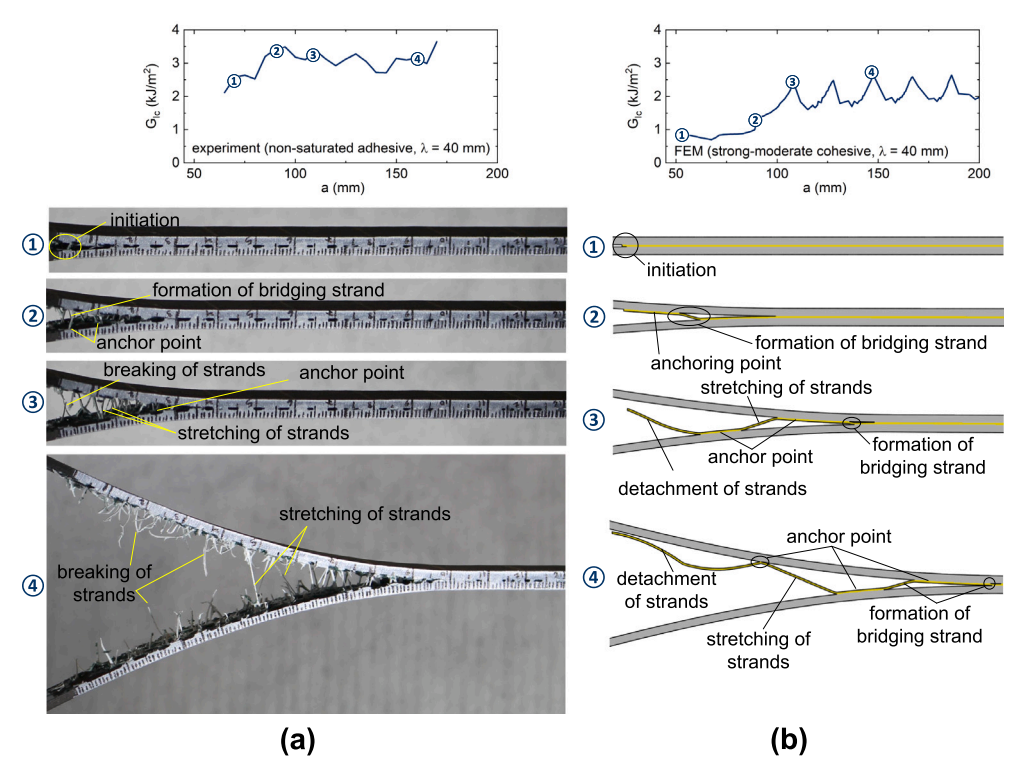


Fig. 6. Bonded joints with hybrid thermoset–thermoplastic bondline, comparison of bridging mechanisms: (a) experiment ( $\lambda = 40$  mm, non-saturated adhesive), (b) FEM ( $\lambda = 40$  mm, strong-moderate cohesive).

cohesive is shown in Fig. 6a and b, respectively. As exemplified by one specimen in Fig. 6a,  $G_{Ic}$  was 2.2 kJ/m<sup>2</sup> (initiation) and 3.3-3.5 kJ/m<sup>2</sup> (propagation). FE model shown in Fig. 6b indicates a lower  $G_{Ic}$  at both initiation and propagation (0.8 kJ/m<sup>2</sup> at initiation, and 2.1 kJ/m<sup>2</sup> at propagation) that is influenced by selected cohesive patterning and insert properties. The experimentally-obtained crackbridging mechanism in DCB specimens with non-saturated adhesive shown in Fig. 6a is generally the same as that with saturated adhesive (Fig. 5a). The mechanisms include crack initiation (1), formation of bridging strands and creation of anchor points (2), stretching of strands ③, and detachment of strand from adherends ④. Fig. 6a shows that the initial increase and the ensuing stable trend of  $G_{Ic}$  are associated with breaking strands from numerous anchor points. The constant amplitude during the oscillation of fracture toughness corresponds strongly to the strand stretching and detachment of strands from composite adherend. The wavy architecture of the thermoplastic insert and proper adhesion between the epoxy adhesive and PA-6 insert provided this stability. Non-saturated adhesive was characterized by the porous microstructure, giving space for the strand to stretch. In terms of modeling, the simulated delamination growth and associated crack-bridging mechanisms in the FE model with strong-moderate cohesive are shown in Fig. 6b. The model was able to simulate the evolution of  $G_{Ic}$  at the initiation (1), crack arrest along with the toughness increase (2), and stable crack propagation (3)-(4). In addition, the higher toughness value during the constant oscillation is reasonably achieved by controlling the magnitude of  $G_c$  in the cohesive elements. Here, the moderate cohesive element with  $G_c = 2.46 \text{ kJ/m}^2$  enables us to reach 1.9 kJ/m<sup>2</sup>.

The enhancement of fracture toughness and simulated mechanisms in FE models of  $\lambda=20$  mm for strong-weak and strong-moderate cohesive are shown in Figs. 7a-c. Models with strong-moderate cohesive outperformed those with strong-weak adhesive in fracture toughness. Nonetheless, crack bridging mechanisms in all FE models can be considered similar: crack initiation ①, formation of bridging strands and creation of anchor points ②, stretching of strands ③, and detachment

of strand from adherends 4. The more extended range of stretching exhibited by the strand is evident due to the use of  $\lambda=40$  mm in the bondline. Thus, the modification of  $\lambda$  is expected to affect the wavelength of oscillation and range of stretching directly.

#### 4.2.4. Energy dissipation in the extrinsic toughening

The force-displacement curves obtained from the models with strong-weak and strong-moderate cohesive/interfacial patterns are shown in Fig. 8a and 8b, respectively. Models with smaller wavelengths  $(\lambda = 20 \text{ mm})$  exhibit early crack initiation than those with larger wavelengths ( $\lambda = 40$  mm). Correspondingly, the elastic energy dissipated by the thermoplastic insert in the models with strong-weak and strongmoderate cohesive are shown in Fig. 8a and 8b, respectively. Here, the elastic energy during the crack-bridging process was characterized by oscillation, regardless of the wavelength or the combination of interface elements. The elastic energy of all models is minimal, with the average value of 0.075-0.10 J ( $\lambda = 20$  mm) and 0.11-0.16 J ( $\lambda = 40$  mm). On the other hand, the plastic energy dissipation is strongly affected by the combination of interface elements, as shown in Fig. 8e and 8f. During delamination growth, models with strong-weak interfacial patterns merely dissipated 0.4-0.5 J of plastic energy, while the models with strong-moderate cohesive could dissipate 1.5-1.7 J of plastic energy (around 3× enhancement). Here, the strong-moderate cohesive allowed a more prolonged stretching of the strands than the strongweak cohesive, contributing to higher plastic energy dissipation and improved fracture toughness.

#### 4.2.5. Parametric studies for optimizing extrinsic toughening

To understand the influence of mechanical properties of the thermoplastic bondline, we varied the elastic modulus E, yield stress  $\sigma_v$ , and ultimate stress  $\sigma_u$  in the models with strong-moderate cohesive and  $\lambda = 40$  mm. Fig. 9 shows the stress–strain curves implemented in ABAQUS. The baseline model (insert-1), as described in Section 3.3, have nominal E of 0.3 GPa,  $\sigma_v$  of 26 MPa, and  $\sigma_u$  of 44 MPa. In the model with insert-

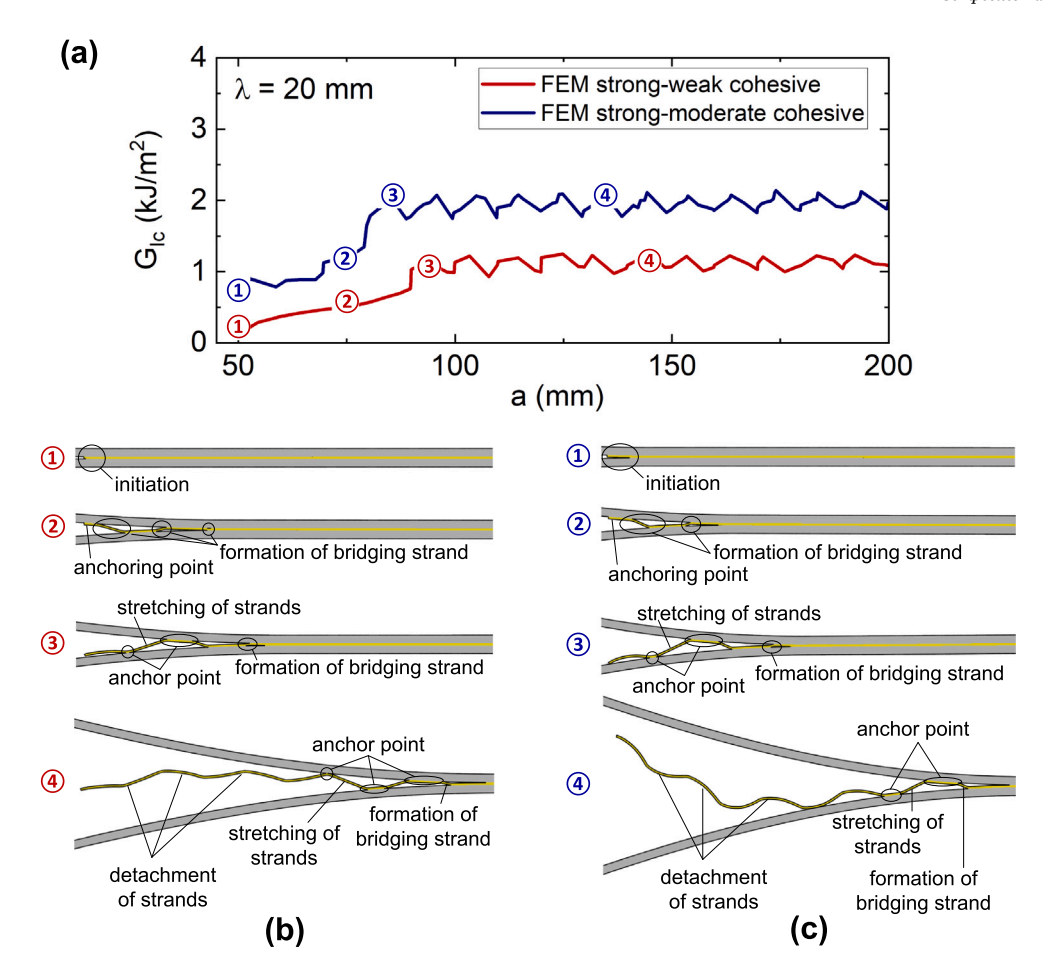


Fig. 7. Bonded joints with thermoset-thermoplastic bondline of  $\lambda = 20$  mm: (a) mode I energy release rate  $G_{Ic}$ , (b) bridging mechanisms in FE model with strong-weak cohesive, (c) bridging mechanisms in FE model with strong-moderate cohesive.

2, we prescribed E=1.4 GPa (stiffer insert) but kept  $\sigma_y$  at 26 MPa and  $\sigma_u$  at 46 MPa, similar to the baseline. In the model with insert-3, we increased E,  $\sigma_y$ , and  $\sigma_u$  to be 1.4 GPa, 52 MPa, and 90 MPa (stiffer, stronger).

Fig. 10a shows that increasing modulus or strength of the thermoplastic bondline does not modify the initial, linear regime or the first peak in the force–displacement curves. During the crack propagation, the effect of using stiffer thermoplastic but keeping the ultimate stress similar is evident. Keeping the strength of the thermoplastic bondline identical to the nominal one, i.e.,  $\sigma_u=46$  MPa, and increasing the modulus to 1.4 GPa was a good strategy to dissipate less elastic energy (see Fig. 10b) but more plastic energy, reaching the value of 6–7 J (see Fig. 10c). Fig. 10d shows that higher plastic energy dissipation by the thermoplastic insert improves  $G_{Ic}$  of up to 4 kJ/m². However, a combination of high modulus and high strength (E=1.4 GPa,  $\sigma_y$ ,  $\sigma_u=90$  MPa) does not necessarily improve the force–displacement curve, energy dissipation (elastic or plastic), or fracture toughness.

Fig. 10e and 10f compare delamination growth in the FE models with insert-2 and insert-3, respectively. Stages ① and ②, which are the initiation and strand formation, are the same between the two models. In Stage ③-④, the interplay between cohesive properties (strong,  $\tau^0$  = 37 MPa,  $G_c$  = 0.51 kJ/m²; moderate,  $\tau^0$  = 19 MPa,  $G_c$  = 2.46 kJ/m²) and insert properties (insert-2 with  $\sigma_y$  = 26 MPa and  $\sigma_u$  = 46 MPa; insert-3 with  $\sigma_y$  = 52 MPa and  $\sigma_u$  = 90 MPa) becomes apparent in the crack bridging mechanism. Fig. 10e shows that although the model with insert-2 displays limited stretching and shorter delamination growth, the model could form bridging strands and anchor points. On the other hand, Fig. 10f shows that although a model with insert-3 exhibits longer stretching and extended delamination growth than a model with insert-2, the detachment was strand as causing long-range

snap that was limiting the formation of bridging strands and anchoring points. One plausible reason for the inability of the model with insert-3 was because the yield point of insert-3 (52 MPa) is higher than the cohesive strength  $\tau^0$  (37 MPa). Allowing the insert to go into the plastic regime, i.e., by making the yield stress lower than cohesive strength  $\tau^0$ , could be an excellent strategy to enhance plastic energy dissipation, thus enabling better crack-bridging and improved fracture toughness.

#### 5. Conclusions

In this work, we proposed a finite element modeling strategy utilizing cohesive zone elements to simulate the crack-bridging mechanisms in bonded joints with hybrid thermoset-thermoplastic bondline under mode I loading. We identified mechanical and interface properties for the model constituents and then validated the models with mode I fracture experiments via double cantilever beam specimens. The proposed models successfully captured the underlying crack-bridging mechanisms responsible for the extrinsic toughening to improve the fracture toughness in bonded joints with hybrid thermoset-thermoplastic bondline of different wavelengths. The models also showed that stretching bridging strands through plastic energy dissipation enhances fracture toughness. A good combination of bondline and cohesive properties can be sought to enable enhanced plastic energy dissipation. More interestingly, a showcase comparison clearly shows the potential of using this proposed model to design the extrinsic bridging, providing a robust pathway toward a tougher adhesively bonded joint design. Although the proposed models are already adequate for advanced designs, further complexity could be integrated into the model to capture more failure mechanisms, such as incorporating the breakage of a thermoplastic insert.

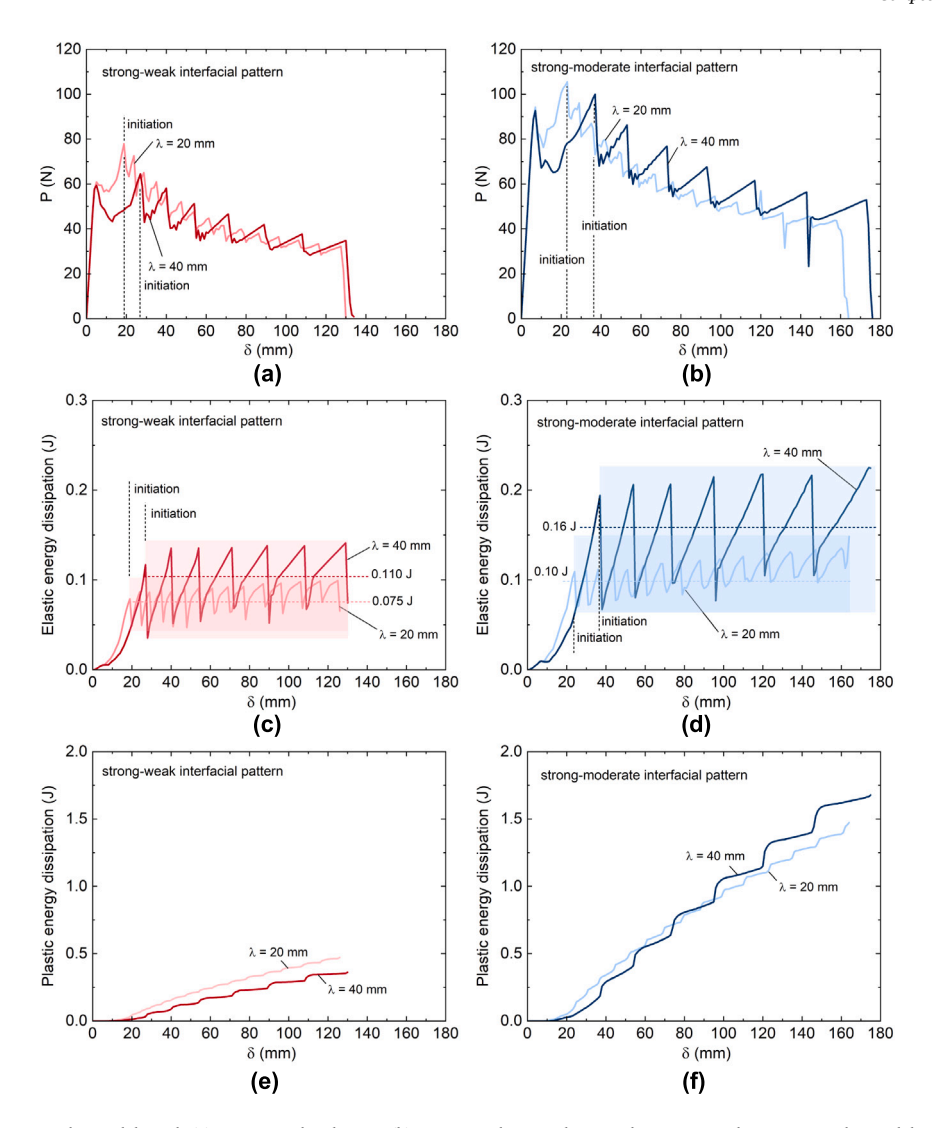


Fig. 8. Force-displacement curves in the models with (a) strong-weak cohesive, (b) strong-moderate cohesive; elastic energy dissipation in the models with (c) strong-weak cohesive, (d) strong-moderate cohesive; plastic energy dissipation in the models with (e) strong-weak cohesive, (f) strong-moderate cohesive.

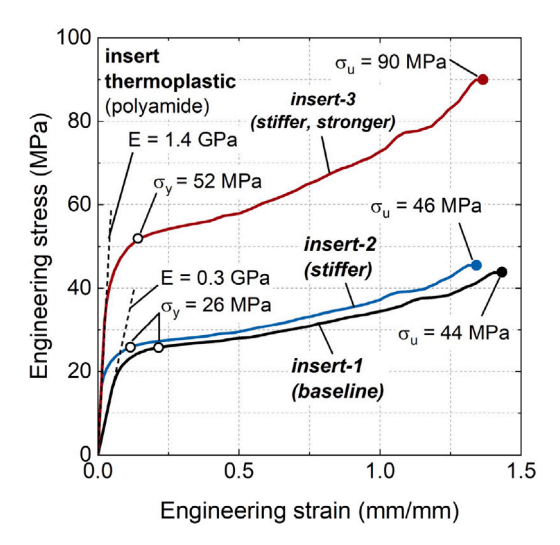


Fig. 9. Stress–strain curves prescribed in the thermoplastic bondline for nominal values (insert-1; E=0.3 GPa,  $\sigma_y=26$  MPa,  $\sigma_u=44$  MPa), insert-2 (E=1.4 GPa,  $\sigma_y=26$  MPa,  $\sigma_u=46$  MPa), and insert-3 (E=1.4 GPa,  $\sigma_y=52$  MPa,  $\sigma_u=90$  MPa).

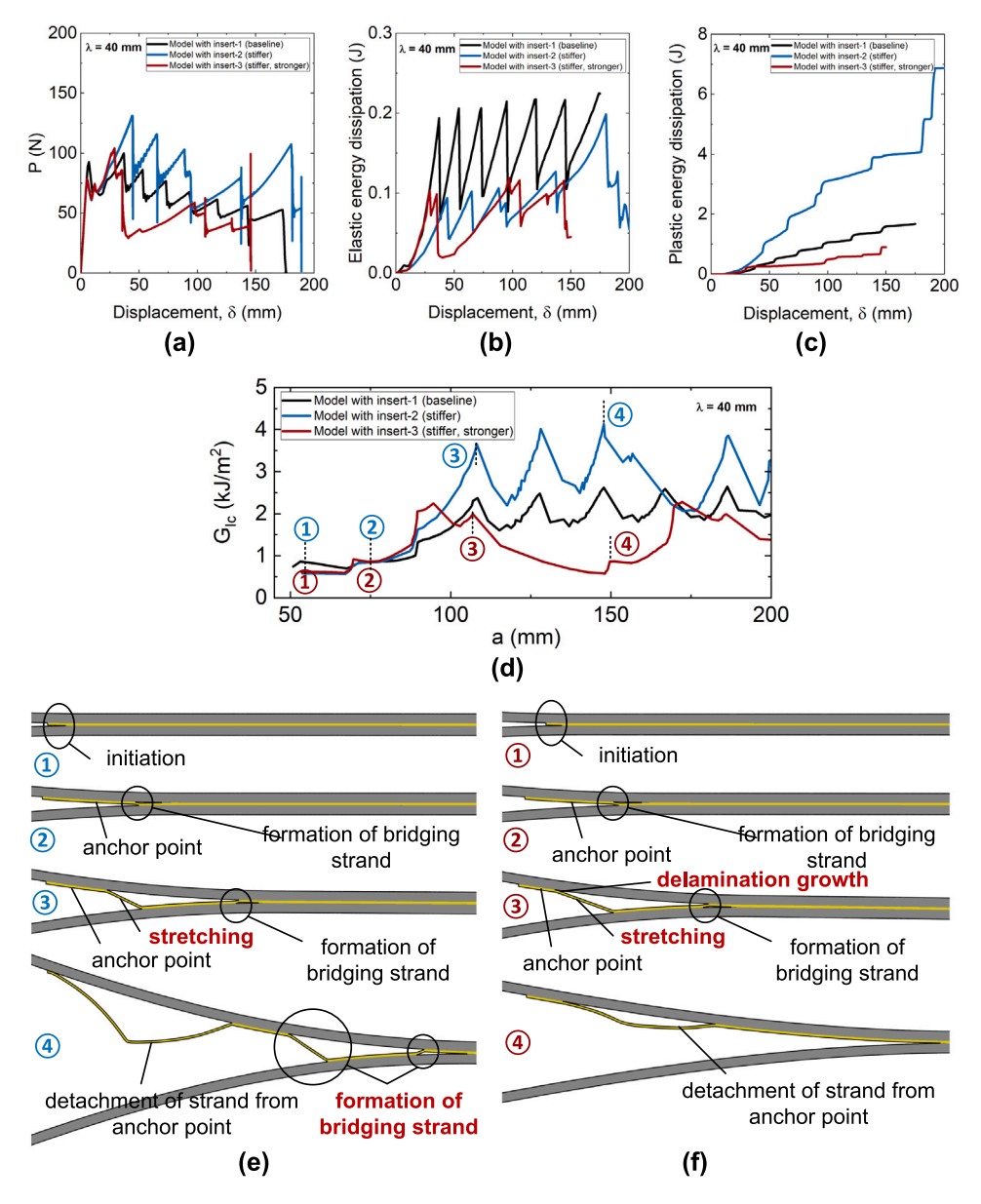


Fig. 10. Influence of the mechanical properties of the thermoplastic bondline on the (a) load–displacement curve, (b) elastic energy dissipation, (c) plastic energy dissipation, (d) mode I energy release rate, (e) delamination growth in DCB model with enhanced stiffness (E = 1.4 GPa,  $\sigma_u = 46$  MPa), (f) delamination growth in DCB model with enhanced stiffness and ultimate strength (E = 1.4 GPa,  $\sigma_u = 90$  MPa).

#### CRediT authorship contribution statement

Arifian Sandovic Perdana: Writing – original draft, Validation, Methodology, Formal analysis, Data curation. Annisa Jusuf: Writing – review & editing, Supervision, Project administration, Funding acquisition, Conceptualization. Arief Yudhanto: Writing – review & editing, Supervision, Methodology, Investigation, Formal analysis, Conceptualization. Gilles Lubineau: Writing – review & editing, Resources, Conceptualization. Ran Tao: Validation, Conceptualization. Bambang Kismono Hadi: Writing – review & editing, Supervision, Conceptualization.

#### Declaration of competing interest

The authors declare that they have no known competing financial interests or personal relationships that could have appeared to influence the work reported in this paper.

#### Acknowledgments

The research was funded by Institut Teknologi Bandung (ITB), Indonesia through the *Penelitian, Pengabdian kepada Masyarakat, dan Inovasi ITB* (Research, Community Service, and Innovation ITB) scheme, Indonesia. Additionally, the support provided by the Office of Sponsored Research (OSR), Saudi Arabia at KAUST (King Abdullah University of Science and Technology) under award number OSR CRG2017-3388 is gratefully acknowledged.

#### Data availability

Data will be made available on request.

#### References

 Soutis C. Fibre reinforced composites in aircraft construction. Prog Aerosp Sci 2005;41(2):143–51.

- [2] Sarfraz MS, Hong H, Kim SS. Recent developments in the manufacturing technologies of composite components and their cost-effectiveness in the automotive industry: A review study. Compos Struct 2021;266:113864.
- [3] Zhang J, Chevali VS, Wang H, Wang C-H. Current status of carbon fibre and carbon fibre composites recycling. Composites B 2020;193:108053.
- [4] Elanchezhian C, Vijaya Ramnath B, Hemalatha J. Mechanical behaviour of glass and carbon fibre reinforced composites at varying strain rates and temperatures. Procedia Mater Sci 2014;6:1405–18.
- [5] Moretti L, Olivier P, Castanié B, Bernhart G. Experimental study and in-situ FBG monitoring of process-induced strains during autoclave co-curing, co-bonding and secondary bonding of composite laminates. Composites A 2021;142:106224.
- [6] Kupski J, Teixeira de Freitas S. Design of adhesively bonded lap joints with laminated CFRP adherends: Review, challenges and new opportunities for aerospace structures. Compos Struct 2021;268:113923.
- [7] Kupski J, Zarouchas D, Teixeira de Freitas S. Thin-plies in adhesively bonded carbon fiber reinforced polymers. Composites B 2020;184:107627.
- [8] Federal Aviation Administration. AC 20-107b composite aircraft structure. 2009.
- [9] Ebnesajjad S. Chapter 5 theories of adhesion. In: Ebnesajjad Sina, editor. Surface treatment of materials for adhesive bonding. 2nd ed.. Oxford: William Andrew Publishing; 2014, p. 77–91.
- [10] Heide-Jørgensen S, Teixeira de Freitas S, Budzik MK. On the fracture behaviour of CFRP bonded joints under mode I loading: Effect of supporting carrier and interface contamination. Compos Sci Technol 2018;160:97–110.
- [11] Maloney K, Fleck N. Toughening strategies in adhesive joints. Int J Solids Struct 2019;158:66–75.
- [12] Yudhanto A, Almulhim M, Kamal F, Tao R, Fatta L, Alfano M, Lubineau G. Enhancement of fracture toughness in secondary bonded CFRP using hybrid thermoplastic/thermoset bondline architecture. Compos Sci Technol 2020:199:108346.
- [13] Kumar S, Wardle BL, Arif MF. Strength and performance enhancement of bonded joints by spatial tailoring of adhesive compliance via 3D printing. ACS Appl Mater Interfaces 2017;9(1):884–91, PMID: 27966344.
- [14] van Innis C, Budzik MK, Pardoen T. Ultra-tough architected adhesive joints for integrated composite processing and bonding. Composites A 2024;177:107949.
- [15] Ritchie RO. The conflicts between strength and toughness. Nature Mater 2011;10:817–22.
- [16] Sills RB, Thouless MD. Cohesive-length scales for damage and toughening mechanisms. Int J Solids Struct 2015;55:32–43, Special Issue Computational and Experimental Mechanics of Advanced Materials, A workshop held at KAUST, Saudi Arabia, July 1-3, 2013.
- [17] Huxford B, Ronan W, Russell BP. Fibre bridging: Continuum modelling of extrinsic toughening in double cantilever beam tests. J Compos Mater 2022;56(21):3307–21.
- [18] Lubineau G, Alfano M, Tao R, Wagih A, Yudhanto A, Li X, et al. Harnessing extrinsic dissipation to enhance the toughness of composites and composite joints: A state-of-the-art review of recent advances. Adv Mater 2024:2407132.
- [19] Alshedayfat A, Wagih A, Yudhanto A, Mahmoud H, Lubineau G. Mode II fatigue characteristics of a composite bonded joint with microstructured adhesive bondline through tailored sacrificial cracks. Composites A 2024;180:108090.
- [20] Hisada S, Minakuchi S, Takeda N. Damage tolerance improvement of composite T-joint under pull-up conditions using an interlocking-fiber-based crack arrester. Compos Struct 2020;253:112792.
- [21] Liu W, Chen P. Theoretical analysis and experimental investigation of the occurrence of fiber bridging in unidirectional laminates under mode I loading. Compos Struct 2021;257:113383.
- [22] Canal LP, Pappas G, Botsis J. Large scale fiber bridging in mode I intralaminar fracture. An embedded cell approach. Compos Sci Technol 2016;126:52–9.
- [23] Tao R, Li X, Yudhanto A, Alfano M, Lubineau G. On controlling interfacial heterogeneity to trigger bridging in secondary bonded composite joints: An efficient strategy to introduce crack-arrest features. Compos Sci Technol 2020;188:107964.

- [24] Pawlik M, Yi LYC, Gunputh U, Le H, Wood P, Lu Y. Surface engineering of carbon fibre/epoxy composites with woven steel mesh for adhesion strength enhancement. Int J Adhes Adhes 2022;114:103105.
- [25] Löbel T, Holzhüter D, Sinapius M, Hühne C. A hybrid bondline concept for bonded composite joints. Int J Adhes Adhes 2016;68:229–38.
- [26] Quan D, Urdániz JL, Rouge C, Ivanković A. The enhancement of adhesivelybonded aerospace-grade composite joints using steel fibres. Compos Struct 2018;198:11–8.
- [27] Lima RAA, Tao R, Bernasconi A, Carboni M, Carrere N, Teixeira de Freitas S. Uncovering the toughening mechanisms of bonded joints through tailored CFRP layup. Composites B 2023;263:110853.
- [28] Pascuzzo A, Yudhanto A, Alfano M, Lubineau G. On the effect of interfacial patterns on energy dissipation in plastically deforming adhesive bonded ductile sheets. Int J Solids Struct 2020;198:31–40.
- [29] Hoshikawa Y, Shirasu K, Higuchi R, Kawagoe Y, Tohmyoh H, Okabe T. Experimental and numerical investigation of the relationship between material defects and elastoplasticity behavior of 3D-printed carbon-fiber-reinforced thermoplastics under compressive loading. Compos Sci Technol 2023;241:110116.
- [30] Garcia R, Prabhakar P. Bond interface design for single lap joints using polymeric additive manufacturing. Compos Struct 2017;176:547–55.
- [31] Islam MS, Prabhakar P. Interlaminar strengthening of multidirectional laminates using polymer additive manufacturing. Mater Des 2017;133:332–9.
- [32] Damodaran V, Castellanos AG, Milostan M, Prabhakar P. Improving the mode-II interlaminar fracture toughness of polymeric matrix composites through additive manufacturing. Mater Des 2018;157:60–73.
- [33] Srinivasan DV, Vassilopoulos AP. Toughening of thick bonded interfaces through architected crack-arresting features. Composites A 2025;188:108575.
- [34] Abdel Monsef S, Ortega A, Turon A, Maimí P, Renart J. An efficient method to extract a mode I cohesive law for bonded joints using the double cantilever beam test. Composites B 2019:178:107424.
- [35] ASTM International. ASTM D5528 standard test method for mode I interlaminar fracture toughness of unidirectional fiber-reinforced polymer matrix composites. 2013. West Conshohocken.
- [36] Blackman B, Kinloch A. Fracture tests on structural adhesive joints. In: Moore DR, Pavan A, Williams JG, editors. Fracture mechanics testing methods for polymers, adhesives and composites. European structural integrity society, vol. 28, Elsevier; 2001, p. 225–67.
- [37] Hoshikawa Y, Kawagoe Y, Ryuzono K, Okabe T. Finite element modeling for cohesive/adhesive failure of adhesive structures with a thermosetting resin. Eng Fract Mech 2024;311:110552.
- [38] Smith M. ABAQUS/standard user's manual, version 6.9. United States: Dassault Systèmes Simulia Corp; 2009.
- [39] Banea MD, da Silva LFM, Campilho RDSG. Mode I fracture toughness of adhesively bonded joints as a function of temperature: Experimental and numerical study. Int J Adhes Adhes 2011;31(5):273–9, Special Issue on Joint Design 2.
- [40] Camanho PP, Dávila CG. Mixed-mode decohesion finite elements for the simulation of delamination in composite materials. NASA; 2002, p. 1–37.
- [41] Morano C, Scagliola M, Bruno L, Alfano M. Crack propagation in adhesive bonded 3D printed polyamide: Surface versus bulk patterning of the adherends. Int J Adhes Adhes 2024;131:103660.
- [42] Lopes Fernandes R, Teixeira de Freitas S, Budzik MK, Poulis JA, Benedictus R. From thin to extra-thick adhesive layer thicknesses: Fracture of bonded joints under mode I loading conditions. Eng Fract Mech 2019;218:106607.
- [43] Li X, Lu S, Lubineau G. Snap-back instability of double cantilever beam with bridging. Int J Solids Struct 2021;233:111150.
- [44] Mohan J, Ivanković A, Murphy N. Mode I fracture toughness of co-cured and secondary bonded composite joints. Int J Adhes Adhes 2014;51:13–22.